KeAi
CHINESE ROOTS
GLOBAL IMPACT

Available online at www.keaipublishing.com/en/journals/journal-of-magnesium-and-alloys/

ScienceDirect

Journal of Magnesium and Alloys 13 (2025) 3713–3724

www.elsevier.com/locate/jma

Full Length Article

Developing a novel high-strength Mg-Gd-Y-Zn-Mn alloy for laser powder bed fusion additive manufacturing process ☆

Qingchen Deng, Zhiyu Chang, Ning Su, Jing Luo, Yaoyuan Liang, Yuhao Jin, Yujuan Wu*, Liming Peng, Wenjiang Ding

National Engineering Research Center of Light Alloy Net Forming and State Key Laboratory of Metal Matrix Composites, School of Materials Science and Engineering, Shanghai Jiao Tong University, Shanghai 200240, China

Received 6 August 2023; received in revised form 30 August 2023; accepted 15 September 2023
Available online 6 November 2023

Abstract

Laser powder bed fusion (LPBF) of Mg alloys mainly focuses on the traditional commercial casting Mg alloys such as AZ91D, ZK60 and WE43, which usually display relatively low tensile strengths. Herein we developed a novel high-strength Mg-12Gd-2Y-1Zn-0.5Mn (wt.%, GWZ1221M) alloy for the LPBF additive manufacturing process, and the evolution of microstructure and mechanical properties from the as-built state to LPBF-T4 and LPBF-T6 states was systematically investigated. The as-built GWZ1221M alloy exhibited fine equiaxed grains with an average grain size of only 4.3 ± 2.2 μm, while the as-cast alloy displayed typical coarse dendrite grains (178.2 ± 73.6 μm). Thus, the as-built alloy showed significantly higher tensile strengths than the as-cast counterpart, and its yield strength (YS), ultimate tensile strength (UTS) and elongation (EL) were 315 ± 8 MPa, 340 ± 7 MPa and 2.7 ± 0.5% respectively. Solution treatment transformed hard and brittle β-$(Mg,Zn)_3(Gd,Y)$ phase into basal X phase and lamellar long period stacking ordered (LPSO) with better plastic deformability, leading to the improvement of EL. Then peak-aging heat treatment introduced numerous nano-sized prismatic β' precipitates inside grains, resulting in the enhancement of YS. Finally, the LPBF-T6 alloy achieved appreciably high strength with YS, UTS and EL of 320 ± 3 MPa, 395 ± 4 MPa and 2.1 ± 0.4% respectively. Both as-built and LPBF-T6 GWZ1221M alloys showed remarkably higher tensile strengths than the as-cast counterparts and as-built commercial Mg alloys, highlighting the great potential of high-strength as-built Mg-Gd based alloys for structural applications.

Keywords: Laser powder bed fusion (LPBF); Mg-Gd-Y-Zn-Mn alloy; High strength; Solution and aging heat treatment; Long period stacking ordered (LPSO).

1. Introduction

As the lightest engineering metal material, magnesium (Mg) alloy is known as "the green engineering material of the 21st century", which has broad application prospects in automobile, rail transportation, aerospace, defense and military equipment [1,2]. The development of high strength and ductility Mg alloys is of great interest for the application of load-bearing components, which is also a perpetual research hotspot [3,4]. At present, more than 90% of Mg alloy products are prepared by ancient casting method [5,6], because Mg alloy usually exhibits poor deformation ability owing to the intrinsic hexagonal close-packed (HCP) crystal structure. However, the following problems are unavoidable when fabricating large components using casting method [7]: (i) low cooling rate due to large melting volume results in coarse grains and poor mechanical properties; (ii) uneven solute and flow fields lead to frequent casting defects such as macrosegregation and shrinkage porosity, so the subsequent plastic deformation is usually used to improve casting defects and enhance mechanical properties; (iii) the research and development cycle is long because of the requirement of special large molds. Besides, the casting process has disadvantages of limited design freedom, low product qualification rate, low material utilization rate, high energy consumption and heavy pollution. Therefore, there is an urgent need to develop new

☆ Peer review under the responsibility of Chongqing University.

* Corresponding author.
E-mail address: wuyj@sjtu.edu.cn (Y. Wu).

https://doi.org/10.1016/j.jma.2023.09.027

manufacturing methods for Mg alloys to overcome the above problems.

Casting process belongs to formative manufacturing, and mechanical processing belonging to subtractive manufacturing is necessary to meet the dimensional and surface accuracy of the products. As a comparison, additive manufacturing (AM) process is a young and thriving advanced manufacturing technology, which prepares components by adding material point by point, track by track, and layer by layer [8,9]. Accordingly, AM process exhibits the following advantages [7]: (i) high cooling rate due to extreme micro-region metallurgical solidification condition results in fine microstructure and high strength; (ii) small melt pool with size of typically hundreds of microns leads to uniform composition distribution and no macro-segregation; (iii) the research and development cycle is short. Moreover, AM process can fabricate any large complex shape theoretically due to the layered slicing, and has high material utilization and high manufacturing accuracy. Using AM to manufacture metal components displays obvious advantages of parts integration, weight reduction, cycle time reduction, serviceability improvement, near-net forming and low material loss. Thus, the adoption of AM for the preparation of Mg alloy components has a promising engineering application [10,11].

Mainstream metal AM technology mainly includes three processes: laser powder bed fusion (LPBF) with powder bed, laser directed energy deposition (LDED) with powder feeding and wire arc additive manufacturing (WAAM) with wire feeding, of which LPBF has the highest cooling rate ($\sim 10^6$ K/s) and manufacturing accuracy ($\pm$ 0.1 mm) [12]. So LPBF of Mg alloys has attracted great attention in recent years despite the flammable and explosive properties of Mg alloy powders. However, the current research on LPBF of Mg alloys mainly focuses on the traditional commercial casting Mg alloy series (e.g. pure Mg [13], AZ91D [14,15], AZ61 [16], ZK60 [17,18], WE43 [19–21]), which faces challenges such as easy formation of coarse columnar grains, easy cracking, many gas pore defects, strength and ductility need to be further improved. Compared with the above commercial Mg alloys, Mg-Gd based rare earth (RE) Mg alloys display two distinct advantages [3]: high room temperature tensile strength (500 MPa versus 300 MPa) and superior heat resistance (the service temperature increases from 150 °C to 300 °C). So high-strength and heat-resistant wrought Mg-Gd-Y-Zn-Mn alloys have been successfully developed in our previous works [3,22,23]. For example, the Mg-12.6Gd-1.3Y-0.9Zn-0.5Mn (wt.%, the entire text is in weight percent) alloy shows ultra-high yield strength (YS) of 543 MPa, ultimate tensile strength (UTS) of 564 MPa but low elongation (EL) of only 1.2% after hot extrusion, 10% cold rolling, 2% cold stretching and aging processes [22], and the Mg-12Gd-2Y-1Zn-0.5Mn (GWZ1221M) alloy exhibits YS of 427 MPa, UTS of 509 MPa and relatively high EL of 5.1% after extrusion and peak-aging treatment [23].

As is well known, Zr element is the common grain refining element in casting Mg-RE alloys due to its high solidification growth restriction factor (GRF, also known as Q value) [24,25]. Zr element can also refine grains significantly of the as-built Mg-Gd based alloys prepared by LPBF [26–28]. Mn element cannot refine grains obviously of the as-cast Mg-RE alloys [29], but can refine grains of the as-extruded alloys owing to the precipitation of α-Mn particles during solution heat treatment [30]. On the other hand, Mn element can enhance the corrosion resistance, and its cost is remarkably lower than that of Zr element [31]. More importantly, Mn can also undergo peritectic reaction with Mg, just the same as Zr, so Mn addition may also produce some grain refinement effects. However, addition of Mn into Mg-Al-Zn based alloys exhibits opposite grain refinement effects: the as-built Mg-8.89Al-0.45Zn-0.19Mn (AZ91D) alloy shows extremely fine uniform equiaxed grains with an average grain size of only 1.2 μm [15], while the as-built Mg-10.6Al-0.6Zn-0.3Mn (AZ111) alloy displays coarse columnar grains parallel to BD with an average grain size of 28 μm [32]. LPBF process has significantly higher cooling rate than conventional casting process, but whether the Mn element can refine the grains of the as-built Mg alloys remains unclear. There is no report on the LPBF of Mn-containing Mg-Gd based alloys until now. Therefore, the GWZ1221M alloy with good combination of strength and ductility is chosen to manufacture customized pre-alloyed powders, then LPBF-AM process is used to print samples in order to characterize the unique microstructure and mechanical properties of the as-built alloy. Precipitation strengthening contributes most to the tensile strength in the Mg-Gd based alloys, so subsequent solution and aging heat treatment are performed to modify microstructure and enhance mechanical properties.

2. Materials and methods

2.1. Powder preparation

Firstly, we prepared large-scale ingots with weight of about 300 kg and diameter of 110 mm by semi-continuous casting. Then centrifugal atomization (Tangshan Weihao Magnesium Powder Co., LTD., China) was used to manufacture pre-alloyed powders through re-melting ingots after removal of surface oxide by turning. The molten metal liquid is spun into droplets by a centrifugal atomizing disk, and then solidified into fine powder in high purity Ar. The vaporization loss of Mg element during LPBF process is inevitable, so the as-built Mg-Gd based alloys usually have higher contents of alloying elements than original powders, especially Gd content is usually 1–2 wt.% higher [26,33]. Therefore, in order to obtain an as-built alloy of target chemical composition, the vaporization loss of Mg element is considered in advance to reduce the Gd content in ingots. The measured chemical compositions of ingot, powder and as-built alloy by inductively coupled plasma atomic emission spectroscopy analyzer (ICPAES, PerkinElmer, Optima^{TM} 7300 DV) are listed in Table 1. The chemical compositions of ingot and powder are close to each other. As expected, the Gd content increased 1.54 wt.% while the contents of other alloying elements increased a little after LPBF process. The actual chemical com-

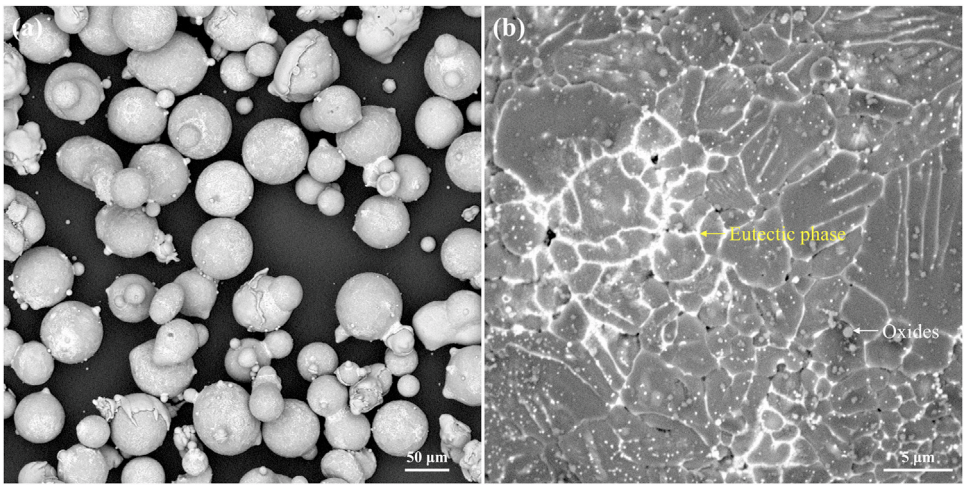

Fig. 1. The morphology of 200–300 mesh pre-alloyed powders.

Table 1
The measured chemical compositions of ingot, powder and as-built alloy.

States	Gd	Y	Zn	Mn	Mg
Ingot	11.19	1.73	1.07	0.53	Bal.
Powder	10.86	1.70	0.96	0.52	Bal.
As-built alloy	12.40	1.77	1.33	0.53	Bal.

position of the as-built alloy is close to the nominal composition of Mg-12Gd-2Y-1Zn-0.5Mn (GWZ1221M).

The morphology of 200–300 mesh pre-alloyed powders is shown in Fig. 1. Most of the powders have a spherical shape, although some satellite powders and irregular-shaped powders still exist (Fig. 1a). The average particle diameter is about 64 μm [33]. The powders exhibit fine equiaxed grain morphology (Fig. 1b) due to the high cooling rate of centrifugal atomization process. The eutectic phase mainly distributes along grain boundaries, and the grain size of powders is about 2–4 μm. Moreover, some fine spherical oxides appear on the surface of powders, which are formed during the inerting process to guarantee the safety during storage, transportation and human handling.

2.2. LPBF and heat treatment processes

A commercial ZRapid iSLM 160 machine (ZRapid Tech Co., LTD, China) equipped with an IPG fiber laser with a wavelength of 1064 nm was used to print samples. The focused diameter of laser spot is about 60 μm. As for metals like Mg or Zn that vaporize easily during LPBF process, laser defocusing can reduce the porosity by decreasing laser energy density and enhancing stability of keyhole inside melt pool. So the build platform is lowered by 1.5 mm to increase the spot size to about 150 μm before printing after powder laying. Based on our previous optimization of laser energy density for Mg-Gd based alloys [26,34], the following process parameters were adopted: laser power is 140 W, scanning speed is 800 mm/s, hatch spacing is 0.1 mm, layer thickness is 0.03 mm, rotation angle between successive layers is 67°, and island scanning strategy is used. The heating temperatures of build platform and powder bed are 200 °C and 120 °C, respectively, in order to reduce temperature gradient and thermal stress accumulation. The amount of powder supplied to each layer which refers to the rising height of powder bed is about 4 times the layer thickness to compensate for the powder loss from powder splashing and depressions in the laser scanning area. We printed two types of samples: cubic samples with cross section of 10 mm × 10 mm for defects and microstructure observation, and tensile blocks with gauge section of 18 mm × 3 mm for tensile tests. Cracking can easily occur during the LPBF of high-strength Mg-Gd based alloys [27,35], and high build height will increase the cracking susceptibility. Thus, the build height of cubic samples and tensile blocks is set to 6 mm to avoid cracking and maintain structural integrity. Besides, one cubic sample with build height of 10 mm was printed to compare cracking susceptibility. The thickness of plate tensile samples is about 1.5 mm, so one tensile block can be cut into four plate tensile samples.

Solution heat treatment was carried out in a muffle furnace held at a set temperature for a certain period of time. After a certain solution time, samples were quickly removed from the muffle furnace and quenched in cold water to remain the solution-treated state in room temperature. Then artificial aging heat treatment was performed in an oil bath at 175 °C or 200 °C. After a certain aging time, samples were also quenched in cold water.

2.3. Microstructure characterization and mechanical performance testing

Optical microscope (OM, Zeiss Axio observer) was used to observe the pore defects inside the as-built samples in brightfield mode and dendrite morphology in the as-cast and casting-T4 samples in polarization mode. The porosity of the as-built sample is calculated by measuring the area fraction of pore defects using OM images with magnification of 25. Scanning electron microscope (SEM, TESCAN MIRA3) was

used to observe powder morphology and secondary phases. Electron backscatter diffraction (EBSD) was used to characterize grain morphology and orientation inside the as-built alloy. Transmission electron microscope (TEM, FEI TECNAI G^2 S-TWIN) was used to determine the prismatic and basal precipitates. The detailed sample preparation process for electron microscope observation can be found in our previous work [26]. The phase constitutions of the samples were measured by X-ray diffraction (XRD). A Poly-functional X-Ray Diffractometer (D8 ADVANCE Da Vinci, Bruker, Germany) equipped with a Cu-Kα radiation source operating at 40 kV and 40 mA was used. The scanning angle ranged from 20° to 60°, and the scanning speed was 1°/min.

Mechanical performance testing includes room temperature tensile test and Vickers hardness test. Tensile test was performed on a WDW-10 s universal tensile tester (TE, Jinan, China) with a constant tensile speed of 0.5 mm/min. An extensometer with a test length of 6 mm was placed into the gauge section of the plate tensile samples to measure engineering strain. At least three parallel tensile tests of samples in one state were conducted to obtain the average values of YS, UTS and EL. Vickers hardness test was performed on an integrated Vickers hardness tester (XHVT-10Z, Shanghai, China) with a load of 49 N and a residence time of 15 s. Each Vickers hardness value was obtained from the averages of at least seven independent measurement values after minimum and maximum values were removed.

3. Results

3.1. XRD analysis

XRD patterns of the GWZ1221M alloy under the powder, as-built and LPBF-T4 states are displayed in Fig. 2. The GWZ1221M powder is composed of α-Mg matrix, β-$(Mg,Zn)_3(Gd,Y)$ secondary phase and a small amount of Y_2O_3 oxides [27]. Compared with the formation of oxides containing Mg, Gd or Zn, the formation enthalpy of Y_2O_3 oxides is the lowest leading to the preferential formation of Y_2O_3 oxides [19]. The melting point of Y_2O_3 oxides is as high as 2410 °C, so Y_2O_3 oxides always exist in the LPBF and subsequent heat treatment processes. LPBF process only re-melts the pre-alloyed powder to form a melt pool and undergoes rapid solidification just like the centrifugal atomization process, so the phase constitution of the as-built alloy is the same as that of powder. After appropriate solution heat treatment, the β-$(Mg,Zn)_3(Gd,Y)$ secondary phase dissolves into the α-Mg matrix or transforms into long period stacking ordered (LPSO) structure. LPSO structure is frequently found in the Mg-RE-Zn based alloys, which can enhance comprehensive mechanical properties [23]. As a result, the LPBF-T4 alloy consists of α-Mg matrix, LPSO structure and Y_2O_3 oxides. Aging heat treatment produces numerous prismatic aging precipitates in the LPBF-T6 alloy, but nano-sized precipitates are difficult to be detected by XRD and will be identified by TEM.

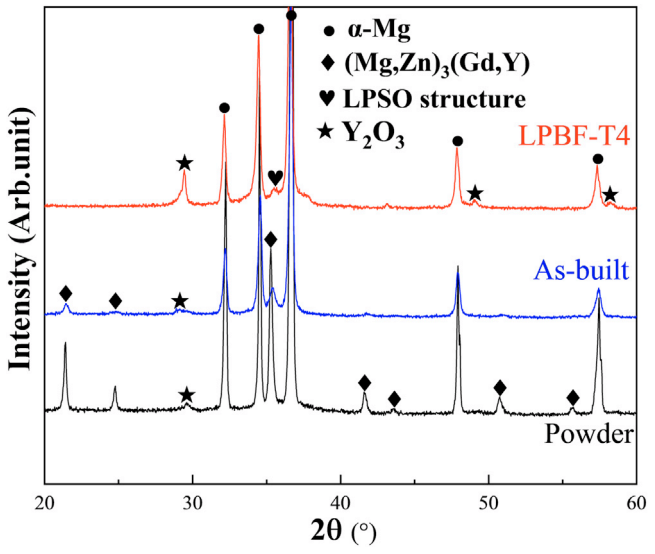

Fig. 2. XRD patterns of the GWZ1221M alloy under the powder, as-built and LPBF-T4 states.

3.2. Microstructure of the as-built GWZ1221M alloy

Fig. 3 shows the macro OM images of the as-built GWZ1221M cubic samples with build height of 6 mm and 10 mm. There are no cracks inside the as-built cubic sample with the low build height of 6 mm, while the as-built cubic sample with the high build height of 10 mm contain obvious cracks. Higher build height will result in greater thermal stress accumulation, leading to higher cracking susceptibility [36]. The cracking cannot be avoided just by adjusting laser energy density, which should be avoided by improving 3D printer or changing alloy composition. A special 3D printer for Mg alloys should have higher preheating temperature of build platform such as 400 °C, or have two lasers with another laser for heating to *in-situ* thermal stress relief. Besides, alloys with higher intrinsic ductility such as G10K alloy [37] should be selected to avoid undesirable cracking. The as-built GWZ1221M alloy inevitably has some minor pore defects due to the keyhole instability and captured by the solidification front [38]. Notably, pore defects at the edge of the as-built sample have obviously larger diameter than those at the interior, which is mainly due to the fact that

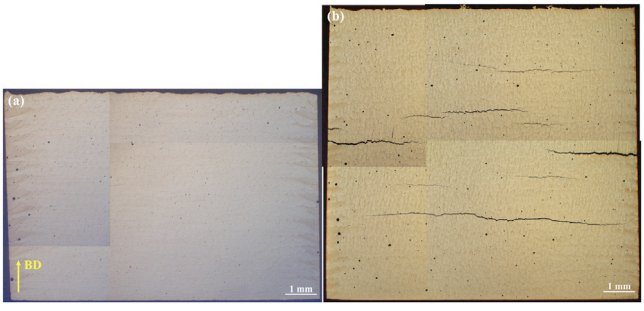

Fig. 3. Macro OM images of the as-built GWZ1221M cubic samples with build height of 6 mm (a) and 10 mm (b).

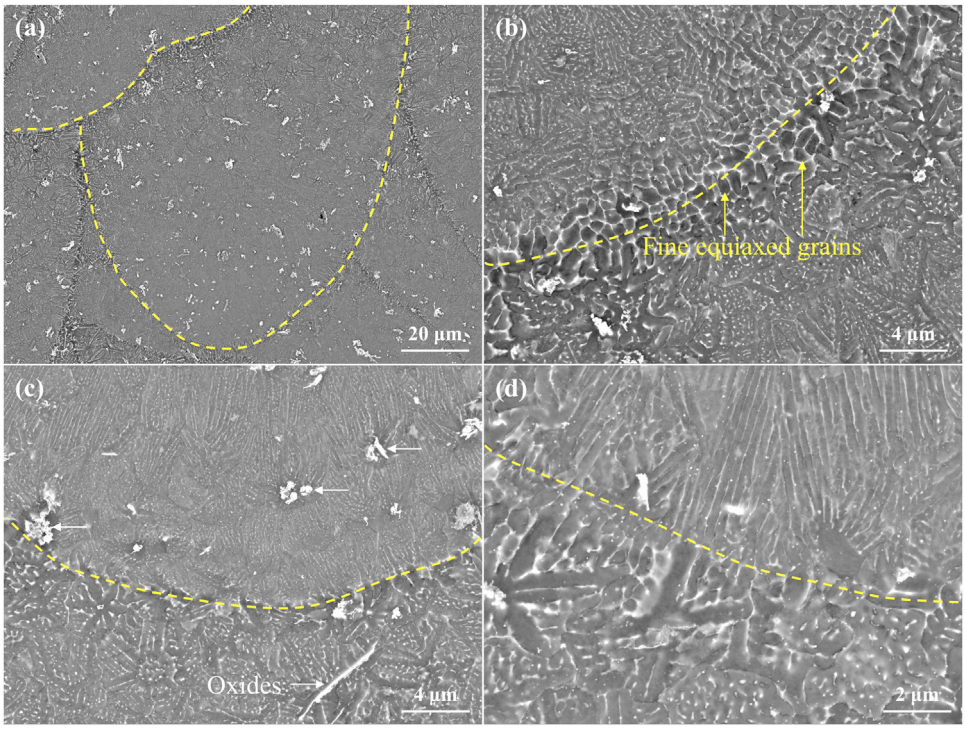

Fig. 4. SEM images of the as-built GWZ1221M alloy.

bidirectional scanning results in increased laser energy density owing to reduced scanning speed at the sample edges. Thanks to the laser defocusing and optimized process parameters, the relative density of the as-built GWZ1221M alloy is as high as 99.85%. As for Mg alloys with low boiling point and high saturated vapor pressure, minor pore defects in the as-built sample are inevitable due to the unavoidable vaporization of Mg element, but optimizing laser energy density can eliminate most pore defects. Besides, optimizing wind filed of the build chamber to remove vaporization products in time, or increasing the preheating temperature of powder bed and build platform, are both beneficial for reducing pore defects. Notably, a small amount of pore defects (<1%) due to the excessive laser energy input will not degrade tensile properties greatly [39], but may be detrimental to fatigue properties.

SEM images of the as-built GWZ1221M alloy are shown in Fig. 4 to reveal the morphology of grains and secondary phases. Melt pool boundaries are indicated by yellow dotted lines. The depth of melt pools is generally greater than the width (Fig. 4a), suggesting the keyhole melting mode. Melt pool boundaries exhibit finest equiaxed grains due to the highest cooling rate (Fig. 4b). In addition to the reticulated β-$(Mg,Zn)_3(Gd,Y)$ secondary phase formed during solidification process along grain boundaries, some fine punctate β-$(Mg,Zn)_3(Gd,Y)$ secondary phases formed by solid state phase transformation also distribute inside grains (Fig. 4b–d). Some parallel lamellae appear inside grains near the melt pool boundaries (Fig. 4c, d), which are caused by the preferential growth of dendrite arms in a given direction [33,37]. Moreover, a few irregular-shaped flaky phases with size of several microns (indicated by white arrows in Fig. 4c) distribute evenly inside the as-built alloy, which are determined to be undesired Y_2O_3 oxides [27]. The Y_2O_3 oxides will degrade mechanical properties and weaken aging precipitation potential, which should be avoided in the future work.

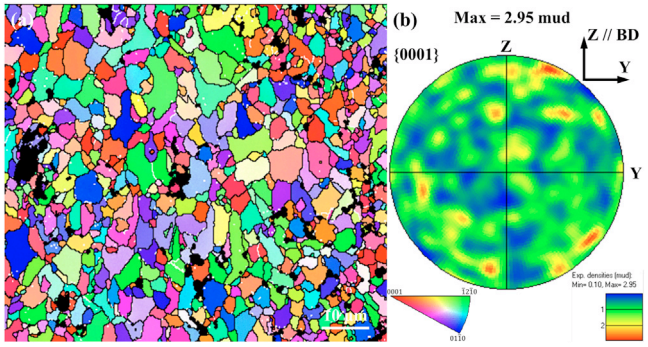

Fig. 5. EBSD grain orientation image (a) and {0001} pole figure (b) of the as-built GWZ1221M alloy.

EBSD observation is conducted to further reveal the morphology and orientation of grains inside the as-built GWZ1221M alloy, as shown in Fig. 5. The as-built alloy is composed of random-orientated fine equiaxed grains with an average grain size of 4.3 ± 2.2 μm (Fig. 5a). No large columnar grains are observed in the as-built GWZ1221M alloy, which are frequently observed in the as-built WE43 [20,40] alloy. Based on {0001} pole figure, the as-built alloy can be considered to be almost free of texture, with the maximum texture intensity of only 2.95 mud (multiple uniform distribution, Fig. 5b).

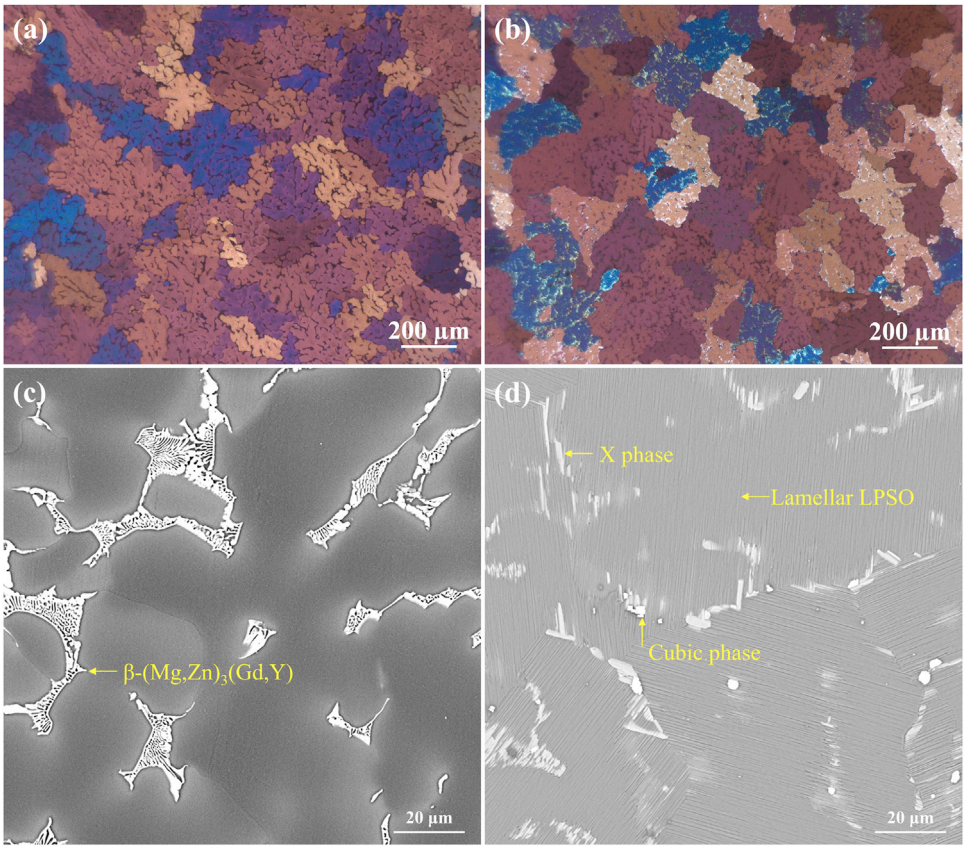

Fig. 6. OM images (a, b) and SEM images (c, d) of the as-cast (a, c) and casting-T4 GWZ1221M (b, d) alloys.

Microstructures of the as-cast and casting-T4 GWZ1221M alloys are also shown in Fig. 6 for comparison. The as-cast alloy exhibits typical dendrite morphology, and black β-$(Mg,Zn)_3(Gd,Y)$ secondary phase distributes along grain boundaries or dendrite arms (Fig. 6a). Coarse bright β-$(Mg,Zn)_3(Gd,Y)$ phase shows typical lamellar structure of eutectic compounds, and forms a semi-continuous network at grain boundaries (Fig. 6b). The average grain size of the as-cast GWZ1221M alloy is measured to be 178.2 ± 73.6 μm, remarkably higher than that of the as-built counterpart.

3.3. Solution and aging heat treatment

According to Ref. [23], the as-cast GWZ1221M alloy should be solution treated at 515 °C for 12 h to obtain the casting-T4 alloy. As shown in Fig. 6b, the casting-T4 alloy still contains coarse dendrite grains, and the average grain size increases a little to 182.4 ± 57.2 μm. Besides, the β-$(Mg,Zn)_3(Gd,Y)$ phase disappear, while a large number of X phase (also named blocky LPSO [41]) and lamellar LPSO structure and a few cubic phase appear (Fig. 6d). X phase nucleates from grain boundaries and grows into the interior of grains, while the growth direction of lamellar LPSO structure inside grains is parallel to the basal plane of grains. Cubic phase is frequently found in the solution treated Mg-RE based alloys [34,42,43], which is determined to be REH_2 rather than MgH_2. Thermodynamically, RE has a lower electronegativity than Mg, resulting in a higher binding propensity to H. Although the cubic phase is detrimental to the mechanical properties, the amount of this phase is relatively low and difficult to be eliminated completely.

Microstructure of the as-built GWZ1221M alloy is significantly different form that of the as-cast counterpart, so the optimal solution heat treatment condition for the as-built alloy should be different from that for the as-cast alloy. Based on our previous optimization of solution heat treatment condition for the as-built Mg-Gd based alloys [27,34], the as-built alloy can be solution treated at lower temperature than the as-cast alloy due to the smaller grains and less secondary phases. Therefore, the optimized solution heat treatment condition for the as-built GWZ1221M alloy is 450 °C × 12 h (LPBF-T4 state), which is the same as that for the as-built GWZ1031K alloy [27].

Fig. 7 shows the SEM images of the LPBF-T4 GWZ1221M alloy. Similar to the microstructure of the casting-T4 alloy, the LPBF-T4 alloy is also free of β-$(Mg,Zn)_3(Gd,Y)$ phase, and mainly contains X phase and lamellar LPSO structure. Besides, a few cubic phase and oxides also distribute randomly in the LPBF-T4 alloy. The average grain size of the LPBF-T4 alloy increases a little to 4.7 ± 1.7 μm. Thermally stable X phase along grain boundaries and lamellar LPSO structure inside grains can inhibit the grain growth greatly during the solution heat treatment, which only occurs in the Mg-RE-Zn based alloys.

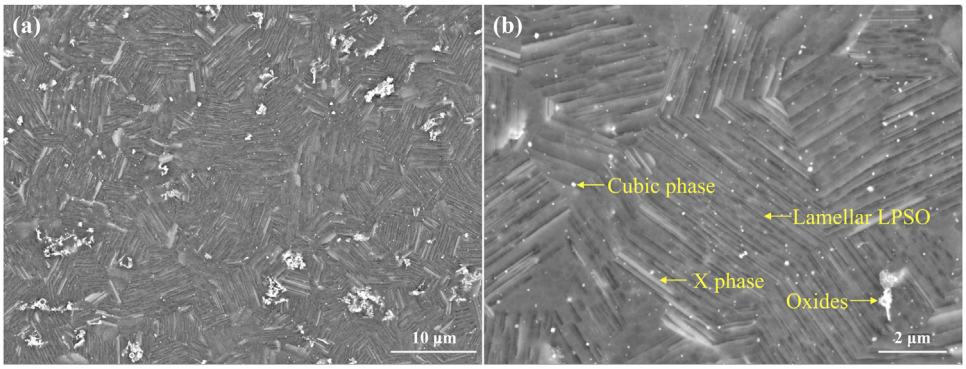

Fig. 7. SEM images of the LPBF-T4 GWZ1221M alloy.

Table 2
The characteristic parameters of the aging hardening curves.

Aging temperature/°C	Initial hardness/HV	Peak-aged hardness/HV	Hardness increment/HV	Time to peak-aged hardness/h
175	96.7 ± 0.4	130.7 ± 1.0	34.0	256
200	96.7 ± 0.4	126.9 ± 1.2	30.2	32

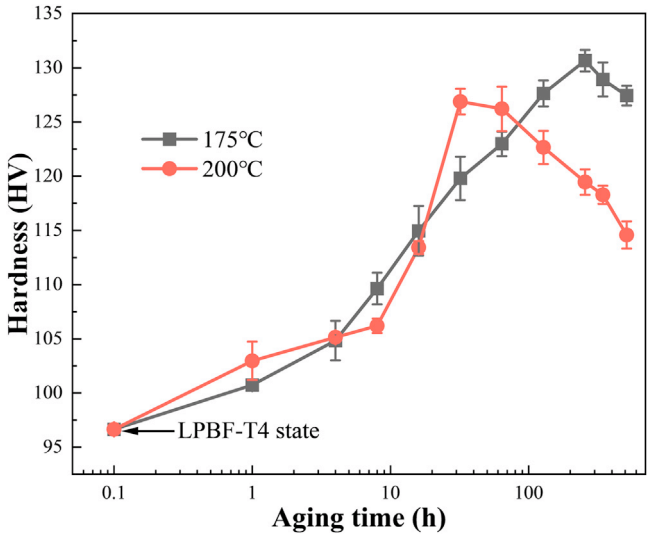

Fig. 8. Aging hardening curves of the LPBF-T4 GWZ1221M alloy at 175 °C and 200 °C.

In order to obtain the peak-aged condition for the LPBF-T4 GWZ1221M alloy, aging hardening curves at 175 °C and 200 °C were measured, as shown in Fig. 8. Table 2 lists the characteristic parameters of the aging hardening curves at 175 °C and 200 °C. The hardness of the as-built GWZ1221M alloy is 112.9 ± 0.9 HV, and it decreases to 96.7 ± 0.4 HV, which is mainly due to the dissolution of hard and brittle β-$(Mg,Zn)_3(Gd,Y)$ phase and release of residual stress. With the extension of aging time, hardness increases steadily and continuously up to a peak, and then gradually decreases. Compared with 200 °C, lower aging temperature of 175 °C can produce stronger precipitation potential and larger hardness increment (34.0 HV versus 30.2 HV), but atomic diffusion becomes slower resulting in the longer time to peak-aged hardness (256 h versus 32 h). The hardness increment is comparable to that of the as-extruded GWZ1221M alloy (33.3 HV [23]), suggesting the excellent aging hardening ability of Mg-Gd based alloys. The superior mechanical properties are pursued in the present work, so the selected aging condition for the LPBF-T4 alloy is 175 °C × 256 h (LPBF-T6 state). 200 °C × 32 h is more suitable as aging heat treatment condition in the future practical engineering applications, which can save cost and energy consumption.

Aging heat treatment at 175 °C basically will not change morphology of grains and secondary phases, so TEM was used to characterize the nano-sized basal 14H-LPSO structure and prismatic aging precipitates in the LPBF-T6 GWZ1221M alloy, as shown in Fig. 9. Both 13 equally spaced diffraction spots between $(0000)_{Mg}$ spot and $(0002)_{Mg}$ spot in the selected area electron diffraction (SAED) pattern (Fig. 9a) and periodic width of about 1.8 nm along C* direction (Fig. 9b, [44]) suggest that the lamellar LPSO structure is the 14H-type with the stacking sequence of ABCACACACBAB. Both X phase and lamellar LPSO structure share the same 14H-LPSO structure, but X phase is transformed from β-$(Mg,Zn)_3(Gd,Y)$ phase and lamellar LPSO structure is precipitated from super-saturated α-Mg matrix during solution heat treatment [34]. Moreover, 14H-LPSO is distributed throughout the X phase, while 14H-LPSO and 2H-Mg are alternately distributed in the lamellar LPSO structure. Fine and dense aging precipitates are uniformly distributed inside the grains (Fig. 9c). Aging precipitates mainly contain β' precipitates with three variants with an angle of 120° to each other (Fig. 9d), which is the most important strengthening phase in the peak-aged Mg-Gd based alloys [6,27,34]. Besides, there are a few hexagonal-shaped structures inside grains, which are formed by the enrichment of solute elements during the early stage of aging process [45].

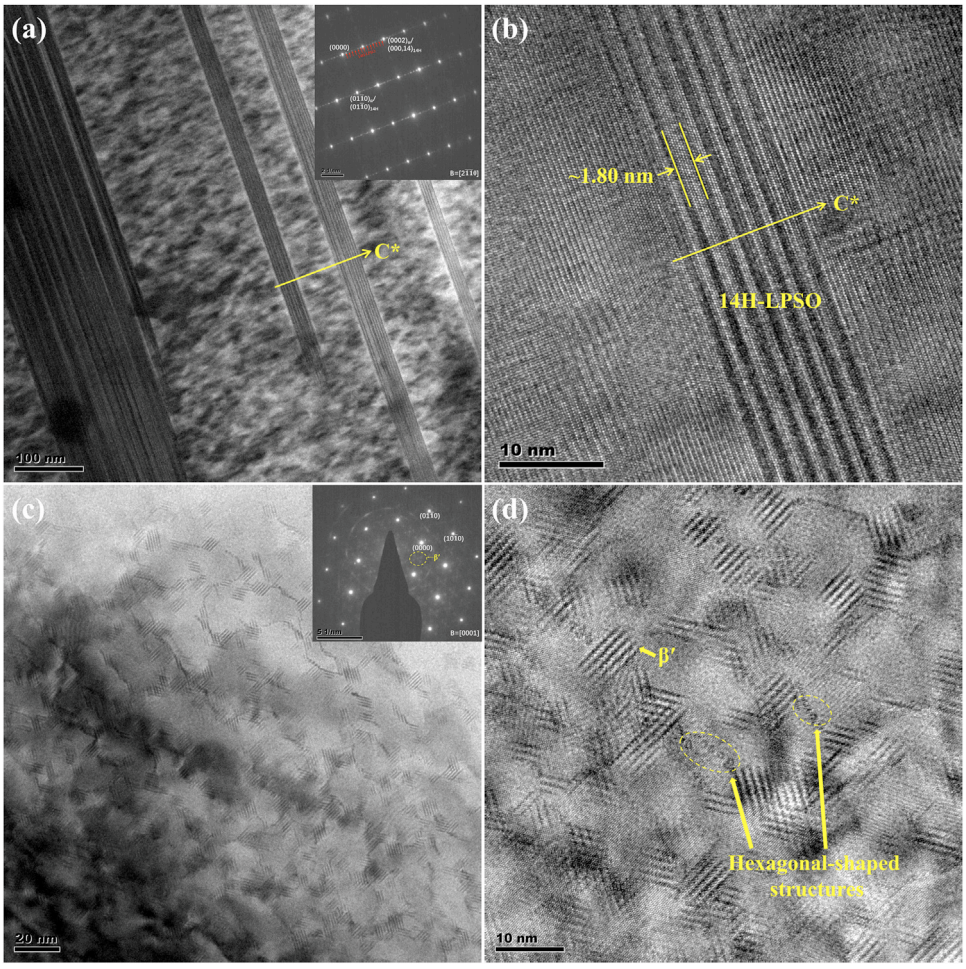

Fig. 9. TEM images and SAED patterns of the LPBF-T6 GWZ1221M alloy: (a, b) basal 14H-LPSO structure and (c, d) prismatic aging precipitates.

3.4. Room temperature tensile properties

The comparison of room temperature tensile properties of the GWZ1221M alloy prepared by LPBF and casting processes under different heat treatment states is displayed in Fig. 10. Obviously, the GWZ1221M alloy prepared by LPBF process under different heat treatment states exhibits significantly higher tensile strengths (YS and UTS) than that prepared by casting process. For example, YS, UTS and EL of the as-built GWZ1221M alloy are 315 ± 8 MPa, 340 ± 7 MPa and 2.7 ± 0.5% respectively, while those of the as-cast counterpart are only 155 ± 2 MPa, 222 ± 6 MPa

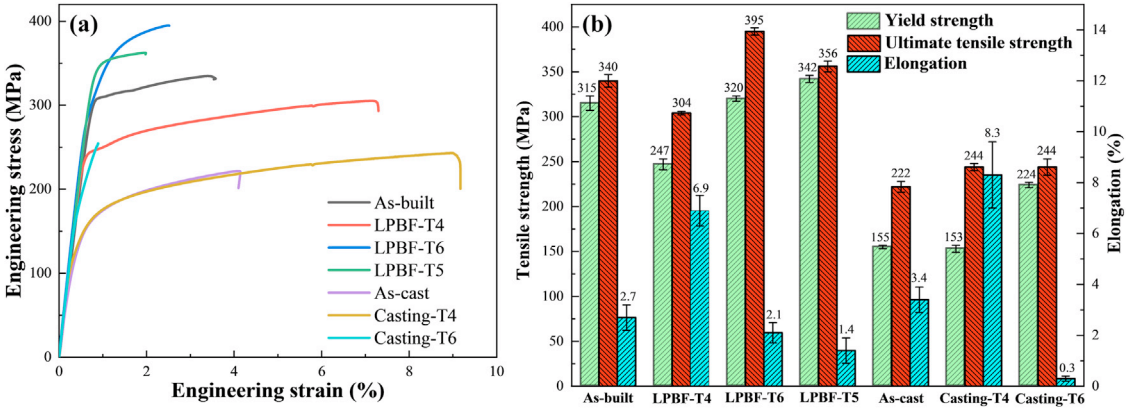

Fig. 10. Room temperature tensile properties of the GWZ1221M alloy prepared by LPBF and casting processes under different heat treatment states: (a) typical tensile curves and (b) average values of YS, UTS and EL.

and 3.4 ± 0.5%. Solution heat treatment can improve tensile ductility of the as-built and as-cast alloys greatly. EL increases from 2.7 ± 0.5% in the as-built state to 6.9 ± 0.6% in the LPBF-T4 state. Besides, solution heat treatment decreases YS and UTS of the as-built alloy, but decreases YS a little and increases UTS of the as-cast alloy. As expected, aging heat treatment can increase YS remarkably but decrease EL greatly at the same time [6,27]. The casting-T4 alloy is artificially aged at 200 °C for 128 h to obtain the casting-T6 alloy. The LPBF-T6 alloy exhibits YS of 320 ± 3 MPa, UTS of 395 ± 4 MPa and EL of 2.1 ± 0.4%, which unexpectedly has simultaneous improved tensile strengths and ductility than the casting-T6 alloy. The LPBF-T5 alloy is defined as the as-built alloy directly aged at 225 °C for 32 h. The as-built alloy contains a lot of β-(Mg,Zn)$_3$(Gd,Y) phase consuming numerous RE atoms, so YS increment from as-built state to LPBF-T5 state is only 27 MPa, which is significantly lower than that from LPBF-T4 state to LPBF-T6 state (73 MPa).

Moreover, we also compare the room temperature tensile properties of the GWZ1221M alloy in the present work with other as-built Mg alloys in the literature [10,14–16,19,20,27,28,34,46–53], as shown in Fig. 11. Compared with other as-built Mg alloys (Mg-Y based, Mg-Al based, Mg-Zn based and Mg-Nd based alloys), the overall mechanical properties of GWZ1221M alloy and Mg-Gd based alloys previously reported by our group [27,28,34] are superior, especially YS. YS of the as-built Mg alloys reported by other groups is less than 300 MPa (Fig. 11a), while YS of the as-built Mg-Gd based alloys ranges from 310 MPa to 345 MPa, which is dependent on alloy composition. The as-built WE43 [19] and AZ91D [15] alloys show extremely fine equiaxed grains with average grain size of only 1.1–1.2 μm, which is smaller than that of the as-built Mg-Gd based alloys, but has a much lower YS. Compared with the as-built WE43 [19] and AZ91D [15] alloys, high YS of the as-built Mg-Gd based alloys mainly comes from secondary phase strengthening of Mg$_3$RE phase and solid solution strengthening of RE elements. High YS is very essential for the critical load-bearing engineering components. The LPBF-T6 GWZ1221M alloy exhibits UTS close to 400 MPa, which is higher than all other as-built Mg alloys (Fig. 11b). It is worth noting that the room temperature tensile properties of the as-built WE43 and AZ91D alloys reported by different groups fluctuate considerably, which needs to be standardized in future work.

4. Discussion

4.1. Microstructure comparison of GWZ1221M alloy prepared by LPBF and casting processes

The as-built GWZ1221M alloy exhibits uniform and fine equiaxed grains with thin reticulated β-(Mg,Zn)$_3$(Gd,Y) secondary phase along grain boundaries (Figs. 4 and 5), while the as-cast counterpart contains coarse dendrite grains with coarse lamellar eutectic compounds along grain boundaries (Fig. 6a and c). Solute element can contribute to grain refinement by generation of constitutional super-cooling zone at the front of solid-liquid interface to restrict grain growth, and its efficiency can be evaluated by the solidification growth restriction factor, known as Q value [24]. Compared with the common grain refinement element Zr with high Q value of 38.29, the Q value of Mn element is only 0.15 [25]. As a result, the average grain size of the as-cast GWZ1221M alloy (~180 μm) is remarkably higher than that of the as-cast Mg-RE alloys containing Zr (about 30–40 μm) [6,26,37]. However, the as-built GWZ1221M alloy (4.3 μm) has an average grain size close to that of the as-built GWZ1031K alloy containing Zr (4.1 μm [27]). Accordingly, high cooling rate during the LPBF process may promote the grain refinement efficiency of Mn element. Fig. 12 shows the TEM characterization results of α-Mn particle. Different from cubic phase of REH$_2$, the α-Mn particle distributed inside grains has smaller size (Fig. 12a) with length and width of about 20 nm and 10 nm respectively, and it appears ellipsoidal morphology. EDS maps confirm the obvious enrichment of Mn element inside the α-Mn particle (Fig. 12b), while other elements exhibit no enrichment. The lattice stripes indicated by white dotted lines pass directly through the α-Mn particle (Fig. 12c), indicating the coherent interface between Mg matrix and α-Mn particle. The interfa-

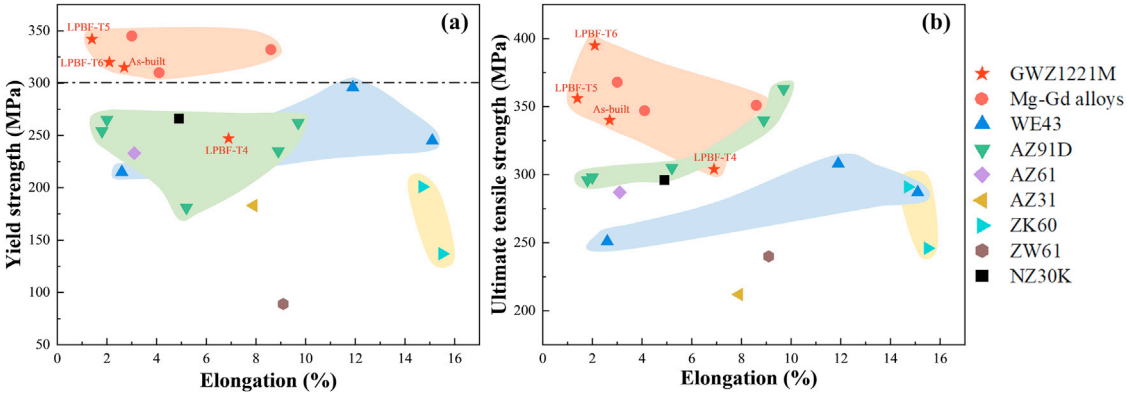

Fig. 11. Comparison of room temperature tensile properties of GWZ1221M alloy in the present work with other as-built Mg alloys in the literature [10,14–16,19,20,27,28,34,46–53]: (a) YS versus EL and (b) UTS versus EL.

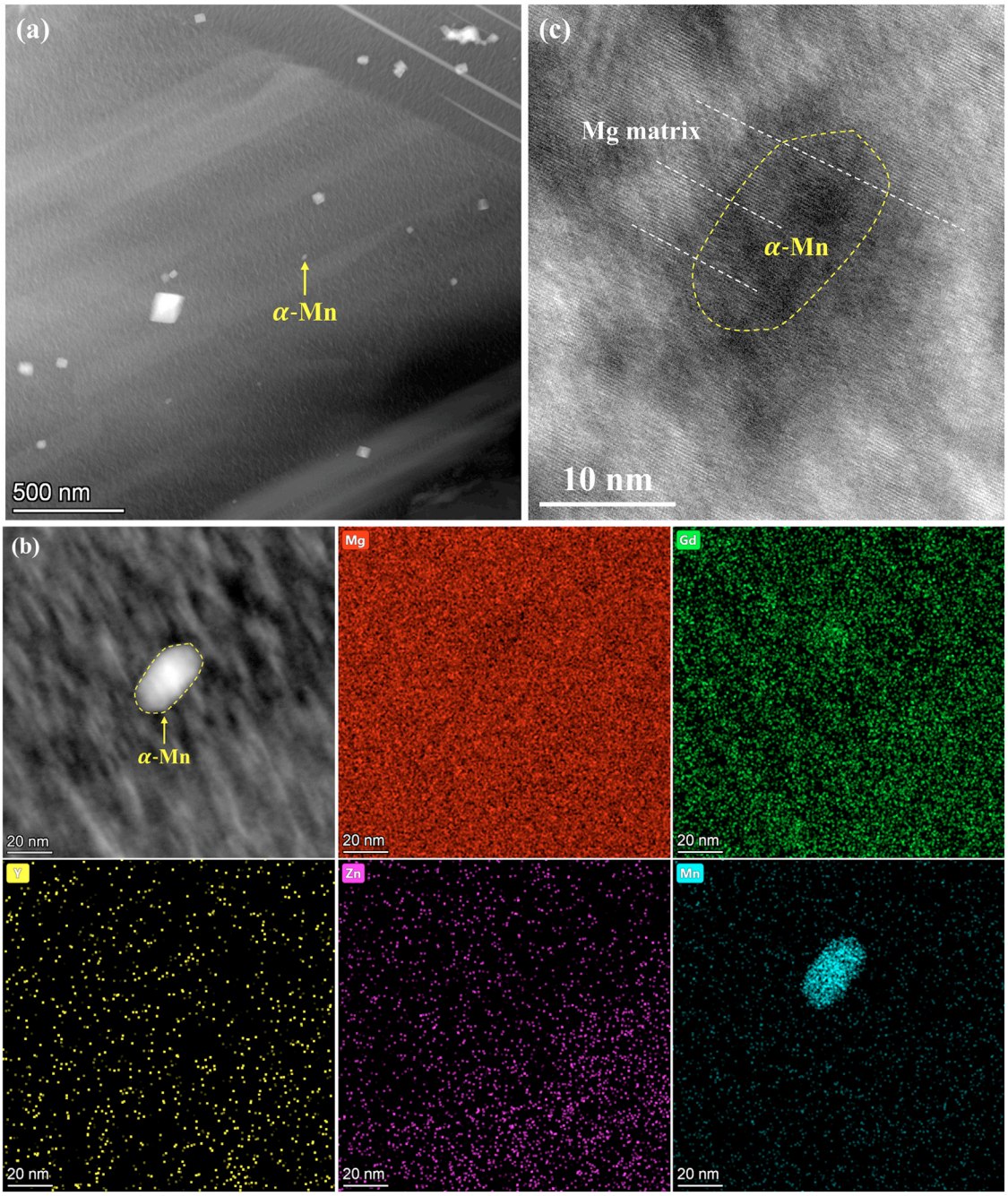

Fig. 12. TEM characterization of α-Mn particle: (a) low magnification HAADF image, (b) high magnification HAADF image and corresponding EDS maps and (c) HRTEM image displaying the coherent interface between Mg matrix and α-Mn particle.

cial energy of coherent interface is lowest, which can reduce the energy barrier for Mg nucleation on α-Mn particle during solidification, confirming the grain refinement ability of α-Mn particle during the LPBF rapid solidification process. Therefore, it is suggested that the as-built Mg-RE alloys prepared by LPBF process should be added with relatively cheap Mn instead of expensive Zr in the future work, which can also refine the grain size to the same level as the Zr addition. Besides, high cooling rate of the LPBF process can cause solute trapping effect and increase the solid solubility of alloying elements in α-Mg matrix [14,26], leading to the less content of β-$(Mg,Zn)_3(Gd,Y)$ phase in the as-built GWZ1221M alloy than the as-cast alloy.

Solution heat treatment of both the as-built and as-cast GWZ1221M alloys transforms the hard and brittle β-$(Mg,Zn)_3(Gd,Y)$ phase into X phase and lamellar LPSO structure with better plastic deformability (Figs. 6 and 7), which is the unique solid state phase transformation of the Mg-RE-Zn alloys [27,34] and improves ductility greatly (Fig. 10). It is noteworthy that the solution temperature of the as-built alloy is obviously lower than that of the as-cast alloy (450 °C < 515 °C), which is beneficial for avoiding undesirable

grain growth and saving energy. This should be attributed to the fact that the smaller grains and less β-(Mg,Zn)$_3$(Gd,Y) phase in the as-built alloy can accelerate atomic diffusion at lower temperature [34]. Then peak-aging heat treatment produces a large amount of dense fine prismatic β' precipitates distributed perpendicularly to the basal 14H-LPSO structure, resulting in the significant improvement of YS. The simultaneous existence of basal LPSO structure and prismatic aging precipitates in the Mg-RE-Zn alloys can contribute more to tensile strengths than the only existence of prismatic aging precipitates in the Mg-RE alloys [6,22]. Fine grains of the as-built GWZ1221M alloy are retained during the post heat treatment, so tensile strengths of the LPBF-T4 and LPBF-T6 alloys are significantly higher than those of the casting-T4 and casting-T6 alloys.

4.2. Strengthening mechanism

As shown in Fig. 10, the as-built GWZ1221M alloy has significantly higher YS and UTS but slightly lower EL than the as-cast counterpart. On the one hand, the as-built alloy exhibits much smaller grains than the as-cast alloy, causing the substantial grain boundary strengthening effect. The grain boundary strengthening effect can be expressed by the Hall-Petch relationship: $\Delta\sigma_{gb} = k(d_1^{-1/2} - d_2^{-1/2})$, where the Hall-Petch constant k is 285 MPa $\times$ $\mu m^{1/2}$ from the as-built and solution-treated GZ112K alloy [34], and d_1 of 4.3 μm and d_2 of 178.2 μm are the average grain sizes of the as-built and as-cast GWZ1221M alloys. As a result, $\Delta\sigma_{gb}$ is calculated to be about 145 MPa. YS of the as-built alloy is 160 MPa higher than that of the as-cast alloy, with grain boundary strengthening effect accounting for about 90%. On the other hand, the content of β-(Mg,Zn)$_3$(Gd,Y) secondary phase in the as-built alloy is lower than that of the as-cast alloy, which will decrease secondary phase strengthening effect but increase solid solution strengthening effect and tensile ductility. However, the ductility of the as-built alloy is slightly lower than that of the as-cast alloy, which may be related to the accumulation of dislocations inside the as-built samples caused by repeated heating and cooling cycles during the LPBF process [54]. The already existence of numerous dislocations in the as-built state will decrease tensile ductility, although it can increase tensile strengths. Besides, pore defects shown in Fig. 3 can cause stress concentration during tensile deformation, deteriorating ductility. It is worth noting that the as-built AZ91D [14], AZ61 [16] and WE43 [19] alloys also exhibit lower ductility than the as-cast counterparts.

The GWZ1221M alloy achieves appreciably high strength after LPBF and subsequent solution and aging heat treatment (LPBF-T6 state), with UTS close to 400 MPa. According to our detailed microstructure characterization, the high tensile strengths of the LPBF-T6 alloy are attributed to the mixed strengthening from grain boundary strengthening with average grain size of only 4.7 μm, precipitation strengthening from dense prismatic β' aging precipitates, and secondary phase strengthening from X phase and lamellar LPSO structure. The main microstructure difference between LPBF-T4 and LPBF-T6 alloys and casting-T4 and casting-T6 counterparts is still the huge grain size difference (4.7 μm versus 182.4 μm), which can bring large YS increment of about 138 MPa. Thus, grain boundary strengthening effect also contribute most to the high strength of the LPBF-T4 and LPBF-T6 alloys.

To sum up, compared with low cooling rate of conventional casting process, high cooling rate of the LPBF process can refine grains greatly, contributing to the significant improvement of tensile strengths in the as-built and subsequent heat-treated alloys. Mg-Gd based alloys prepared by LPBF process exhibit distinct advantages over commercial Mg alloys in terms of mechanical properties, which should be vigorously developed in the future. Besides, alloys in the appropriate heat treatment states should be selected to meet the needs of different practical applications.

5. Conclusions

(1) The as-built GWZ1221M alloy exhibited fine equiaxed grains (4.3 $\pm$ 2.2 μm) with thin β-(Mg,Zn)$_3$(Gd,Y) phase due to the high cooling rate of the LPBF process, while the as-cast alloy showed typical coarse dendrite grains (178.2 $\pm$ 73.6 μm) with coarse lamellar eutectic compounds, demonstrating that relatively cheap Mn can be used to replace expensive Zr as a grain refiner during the LPBF of Mg-Gd based alloys.

(2) Solution heat treatment transformed hard and brittle β-(Mg,Zn)$_3$(Gd,Y) phase into basal X phase and lamellar LPSO with better plastic deformability, then peak-aging treatment introduced numerous prismatic β' precipitates.

(3) YS, UTS and EL of the as-built alloy were 315 $\pm$ 8 MPa, 340 $\pm$ 7 MPa and 2.7 $\pm$ 0.5% respectively, and these values were improved to 320 $\pm$ 3 MPa, 395 $\pm$ 4 MPa and 2.1 $\pm$ 0.4% in the LPBF-T6 alloy. Both as-built and LPBF-T6 GWZ1221M alloys showed remarkably higher tensile strengths (YS and UTS) than the as-cast counterparts and as-built commercial Mg alloys

Declaration of Competing Interest

The authors declare that they have no known competing financial interests or personal relationships that could have appeared to influence the work reported in this paper.

Acknowledgement

The present work was supported by the National Key Research and Development Program of China (No. 2021YFB3701000) and the National Natural Science Foundation of China (Nos. 51971130, 52201129, U21A2047, 51821001, U2037601).

References

[1] G. Wu, C. Wang, M. Sun, W. Ding, J. Magnes. Alloys 9 (2021) 1–20.
[2] J. Song, J. Chen, X. Xiong, X. Peng, D. Chen, F. Pan, J. Magnes. Alloys 10 (2022) 863–898.

[3] N. Su, Y. Wu, Q. Deng, Z. Chang, Q. Wu, Y. Xue, K. Yang, Q. Chen, L. Peng, Mater. Sci. Eng. A 810 (2021) 141019.
[4] X. Xue, Y. Wu, N. Su, X. Heng, Q. Deng, Z. Chang, L. Peng, Mater. Charact. 170 (2020) 110701.
[5] Z. Chang, Q. Deng, Q. Lan, J. Feng, D. Li, B. Liu, Y. Wu, L. Peng, W. Ding, Mater. Sci. Eng. A 848 (2022) 143287.
[6] W. Rong, Y. Wu, Y. Zhang, M. Sun, J. Chen, L. Peng, W. Ding, Mater. Charact. 126 (2017) 1–9.
[7] L. Peng, Q. Deng, Y. Wu, P. Fu, Z. Liu, Q. Wu, K. Chen, W. Ding, Acta Metall. Sin. 59 (2023) 31–54.
[8] B. Lu, D. Li, X. Tian, Engineering 1 (2015) 85–89.
[9] C. Zhang, Z. Li, J. Zhang, H. Tang, H. Wang, J. Magnes. Alloys (2023), doi:10.1016/j.jma.2023.1002.1005.
[10] W. Xu, P. Fu, N. Wang, L. Yang, L. Peng, J. Chen, W. Ding, J. Magnes. Alloys (2022), doi:10.1016/j.jma.2022.1007.1005.
[11] K. Li, C. Ji, S. Bai, B. Jiang, F. Pan, J. Mater. Sci. Technol. 154 (2023) 65–93.
[12] Z. Zeng, M. Salehi, A. Kopp, S. Xu, M. Esmaily, N. Birbilis, J. Magnes. Alloys 10 (2022) 1511–1541.
[13] C.C. Ng, M.M. Savalani, M.L. Lau, H.C. Man, Appl. Surf. Sci. 257 (2011) 7447–7454.
[14] K. Wei, M. Gao, Z. Wang, X. Zeng, Mater. Sci. Eng. A 611 (2014) 212–222.
[15] X. Li, X. Fang, S. Wang, S. Wang, M. Zha, K. Huang, J. Magnes. Alloys (2022), doi:10.1016/j.jma.2022.1006.1004.
[16] S. Liu, W. Yang, X. Shi, B. Li, S. Duan, H. Guo, J. Guo, J. Alloys Compd. 808 (2019) 151160.
[17] J. Liu, B. Yin, Z. Sun, P. Wen, Y. Zheng, Y. Tian, Mater. Lett. 301 (2021) 130283.
[18] J. Liang, Z. Lei, Y. Chen, S. Wu, X. Chen, M. Jiang, S. Cao, Mater. Sci. Eng. A 839 (2022) 142858.
[19] H. Hyer, L. Zhou, G. Benson, B. McWilliams, K. Cho, Y. Sohn, Addit. Manuf. 33 (2020) 101123.
[20] B. Yin, J. Liu, B. Peng, M. Zhou, B. Liu, X. Ma, C. Wang, P. Wen, Y. Tian, Y. Zheng, J. Magnes. Alloys (2022), doi:10.1016/j.jma.2022.1009.1016.
[21] F. Attarzadeh, E. Asadi, J. Magnes. Alloys 10 (2022) 2118–2136.
[22] X. Heng, Y. Zhang, W. Rong, Y. Wu, L. Peng, Mater. Des. 169 (2019) 107666.
[23] N. Su, X. Xue, H. Zhou, Y. Wu, Q. Deng, K. Yang, Q. Chen, B. Chen, L. Peng, Mater. Charact. 165 (2020) 110396.
[24] D.H. StJohn, M. Qian, M.A. Easton, P. Cao, Acta Mater. 59 (2011) 4907–4921.
[25] Y. Ali, D. Qiu, B. Jiang, F. Pan, M.X. Zhang, J. Alloys Compd. 619 (2015) 639–651.
[26] Q. Deng, Y. Wu, Y. Luo, N. Su, X. Xue, Z. Chang, Q. Wu, Y. Xue, L. Peng, Mater. Charact. 165 (2020) 110377.
[27] Q. Deng, Y. Wu, Q. Wu, Y. Xue, Y. Zhang, L. Peng, W. Ding, Addit. Manuf. 49 (2022) 102517.
[28] P. Fu, N. Wang, H. Liao, W. Xu, L. Peng, J. Chen, G. Hu, W. Ding, Trans. Nonferr. Met. Soc. China 31 (2021) 1969–1978.
[29] K. Wang, J. Wang, X. Dou, Y. Huang, N. Hort, S. Gavras, S. Liu, Y. Cai, J. Wang, F. Pan, J. Mater. Sci. Technol. 52 (2020) 72–82.
[30] Y. Zhao, D. Zhang, J. Xu, S. Zhong, B. Jiang, F. Pan, Intermetallics 132 (2021) 107163.
[31] C. Xu, T. Nakata, G.H. Fan, X.W. Li, G.Z. Tang, L. Geng, S. Kamado, J. Mater. Sci. 54 (2019) 10473–10488.
[32] Z. Zeng, S. Choudhary, M. Esmaily, F. Benn, T. Derra, Y. Hora, A. Kopp, A. Allanore, N. Birbilis, npj Mater. Degrad., 6 (2022) 32.
[33] Q. Deng, Y. Wu, N. Su, Z. Chang, J. Chen, L. Peng, W. Ding, Addit. Manuf. 44 (2021) 102036.
[34] Q. Deng, Y. Wu, W. Zhu, K. Chen, D. Liu, L. Peng, W. Ding, Mater. Sci. Eng. A 829 (2022) 142139.
[35] Q. Deng, X. Wang, Q. Lan, Z. Chang, Z. Liu, N. Su, Y. Wu, D. Liu, L. Peng, W. Ding, Mater. Charact. 190 (2022) 112071.
[36] P. Mercelis, J.P. Kruth, Rapid Prototyp. J. 12 (2006) 254–265.
[37] Q. Deng, Y. Zhang, Z. Liu, Z. Chang, N. Su, Y. Wu, L. Hao, L. Peng, W. Ding, J. Alloys Compd. 910 (2022) 164863.
[38] L. Wang, Y. Zhang, H.Y. Chia, W. Yan, npj Comput. Mater. 8 (2022) 22.
[39] H. Gong, K. Rafi, H. Gu, G.D. Janaki Ram, T. Starr, B. Stucker, Mater. Des. 86 (2015) 545–554.
[40] M. Esmaily, Z. Zeng, A.N. Mortazavi, A. Gullino, S. Choudhary, T. Derra, F. Benn, F. D'Elia, M. Müther, S. Thomas, A. Huang, A. Allanore, A. Kopp, N. Birbilis, Addit. Manuf. 35 (2020) 101321.
[41] J.M. Meier, J. Caris, A.A. Luo, J. Magnes. Alloys 10 (2022) 1401–1427.
[42] Z. Zhang, L. Peng, X. Zeng, P. Fu, W. Ding, Mater. Charact. 60 (2009) 555–559.
[43] Q. Peng, Y. Huang, J. Meng, Y. Li, K.U. Kainer, Intermetallics 19 (2011) 382–389.
[44] Y. Yang, C. Ling, Y. Li, S. Peng, D. Xie, L. Shen, Z. Tian, C. Shuai, J. Mater. Sci. Technol. 144 (2023) 1–14.
[45] Y. Zhang, W. Rong, Y. Wu, L. Peng, J.F. Nie, N. Birbilis, J. Alloys Compd. 777 (2019) 531–543.
[46] N.A. Zumdick, L. Jauer, L.C. Kersting, T.N. Kutz, J.H. Schleifenbaum, D. Zander, Mater. Charact. 147 (2019) 384–397.
[47] X. Niu, H. Shen, J. Fu, J. Feng, Mater. Des. 206 (2021) 109787.
[48] K. Nopová, J. Jaroš, O. Červinek, L. Pantělejev, S. Gneiger, S. Senck, D. Koutný, Appl. Sci. 13 (2023) 1377.
[49] C. Chang, H. Liao, L. Yi, Y. Dai, S.C. Cox, M. Yan, M. Liu, X. Yan, Adv. Powder Mater. 2 (2023) 100097.
[50] A. Pawlak, P.E. Szymczyk, T. Kurzynowski, E. Chlebus, Rapid Prototyp. J. 26 (2019) 249–258.
[51] J. Liang, Z. Lei, Y. Chen, W. Fu, S. Wu, X. Chen, Y. Yang, J. Alloys Compd. 898 (2022) 163046.
[52] J. Liang, S. Wu, Z. Lei, Y. Chen, X. Zhang, B. Li, M. Jiang, Y. Chen, Mater. Charact. 194 (2022) 112361.
[53] C. Chen, C. Ling, Y. Shao, Y. Yang, D. Wang, C. Shuai, J. Alloys Compd. 947 (2023) 169555.
[54] G. Wang, H. Ouyang, C. Fan, Q. Guo, Z. Li, W. Yan, Z. Li, Mater. Res. Lett. 8 (2020) 283–290.